Antireflection Substrates for Determining the Number of Layers of Few-Layer Hexagonal Boron Nitride Films and for Visualizing Organic Monolayers

Hattori, Yoshiaki
Taniguchi, Takashi
Watanabe, Kenji
Kitamura, Masatoshi

(Citation)
ACS Applied Nano Materials,6(23):21876-21886

(Issue Date)
2023-10-29

(Resource Type)
journal article

(Version)
Accepted Manuscript

Antireflection Substrate for Determining the Number of Layers of Few-Layer Hexagonal Boron Nitride Films and for Visualizing Organic Monolayers.

*Yoshiaki Hattori[1] *, Takashi Taniguchi[2], Kenji Watanabe[3], and Masatoshi Kitamura[1] ***

[1] Department of Electrical and Electronic Engineering, Kobe University, 1-1, Rokkodai-cho, Nada, Kobe, 657-8501, Japan

[2] International Center for Materials Nanoarchitectonics, National Institute for Materials Science, 1-1 Namiki, Tsukuba 305-0044, Japan

[3] Research Center for Functional Materials, National Institute for Materials Science, 1-1 Namiki, Tsukuba 305-0044, Japan

Corresponding author:

*Email: hattori@eedept.kobe-u.ac.jp, **Email: kitamura@eedept.kobe-u.ac.jp

ABSTRACT:

Visualization of layered materials with atomic-scale thickness by optical interference with a low-reflection substrate has been widely used to identify the exfoliated thin flakes. However, the identification of optically transparent films with an atomic-scale thickness, such as hexagonal boron nitride (hBN), requires a substrate with reflectance lower than a few percent. Although several types of multilayer antireflection (AR) substrates for identification have been developed, the lack of established optical design limits the layer structure of AR coatings. In this study, the reflection circle diagram-based design of AR coatings with a layer of arbitrary materials on top is proposed. AR substrates with diverse materials on top would visualize the various organic monolayers formed on substrates with chemical bonding. As an experimental demonstration, Si substrates with optically designed double-layer AR coating of SiN_x and SiO_2 were assessed by reflection spectroscopy and employed to visualize exfoliated monolayer hBN film. As a result, the presence of the monolayer films on Si/SiN_x (50 nm)/SiO_2 (25 nm) was directly identified in the image photographed by the commercial camera without an optional optical filter and image processing. Additionally, the use of a narrow band-pass filter enhanced the optical contrast of the monolayer hBN up to 17% at 470 nm and enabled easy determination of the number of layers in few-layer hBN flakes.

KEYWORDS: hBN, 2D materials, organic monolayers, antireflection substrate, circle diagram, optical interferometry.

1. INTRODUCTION

Functional organic and inorganic films with an atomic-scale thickness have been applied in electronic devices, where ultra-thin films are chemically or mechanically formed on a substrate at desired positions. However, a problem associated with the process is the detection of ultra-thin films. They are usually difficult to directly observe with an optical microscope because of poor visibility. Therefore, they have been characterized by X-ray or infrared spectroscopy,[1] X-ray reflectivity,[2] ellipsometry,[3] and measurement of physical change of the surface properties, such as contact angle[4] and work function[5] for the formation of the ultra-thin films.

Recently, the visualization of ultra-thin films by interference with an optically designed substrate with antireflection (AR) coating has been studied.[6–18] Optically transparent ultra-thin films on the AR substrate are easily identified in the microscopic image photographed at atmospheric pressure by a commercial digital camera, where an imaging camera detects the difference in reflection at the front surface between the film on the substrate (R_f) and the bare substrate without the film (R_{sub}). The ultra-thin films are visualized in the image with the optical contrast (C) defined as ($R_f/R_{sub} - 1$).[6, 7] Therefore, the use of a substrate with a low R_{sub} increases visibility. Si substrates with a SiO_2 film with an optically designed thickness, which has a minimum R of ~10% at a certain wavelength (λ), have been widely used for visualizing monolayer graphene and other layered materials.[8, 9] However, a substrate with a smaller R_{sub} (less than a few percent) is needed to visualize optically transparent films with an atomic-scale thickness, such as hexagonal boron nitride (hBN),[6, 7]graphene oxide[10] and organic monolayer films.[11,12] Since the technique principally detects optical surface changes on substrates, it can be applied not only to the visualization of ultra-thin films, but also to the detection of several kinds of proteins[12] and the analysis of oxidation-reduction reactions.[13]

The optical design and fabrication of a substrate with low R_{sub} are the essential parts of the visualization technique. One of the proposed substrates has triple-layer AR coatings with an Au surface.[6, 11, 13–15] In this configuration, a thin Au film is deposited on a thermally oxidized Si substrate with an adhesive layer of Cr,[6, 13] Ti,[14, 15] or MoO_3[11]. The typical optimized thickness of the Au layer, adhesive layer, and SiO_2 layer in the AR coatings are ~10 nm, ~1 nm, and ~90 nm, respectively.[6, 11, 13–15] We have demonstrated the visualization of exfoliated monolayer hBN flakes[6, 7] and organic alkanethiol monolayer on the substrate,[11] where the optimum thickness of each layer was determined by calculating the theoretical R_{sub} for various thickness combinations using the well-known transfer matrix method.[19, 20] Through these studies, we have empirically found that the thickness and optical properties of an ultra-thin adhesive layer have a great effect on R_{sub}. However, little study focusing on the adhesive layer has been conducted.

Desired in the visualization technique are stability and flatness of the top layer of the AR coatings. To improve the flatness of the triple-layer AR coatings, it is effective to increase the thickness of the top Au layer. This is due to the surface roughness of such thin Au films with a thickness of less than 10 nm being larger than that of thicker films due to nucleation in the initial stage of growth.[6, 21–23] However, increasing the thickness of the top Au film in the triple-layer coatings results in increased R_{sub}, even if the thickness of the adhesive layer and SiO_2 are adjusted. Therefore, precise thickness control of both the Au layer and the adhesive layer is currently required for the AR coating.

Regarding the thickness of the top Au layer in AR substrates, Syahir et al. have demonstrated the optical detection of the organic monolayer of 1-Amino-8-octanethiol on an Au film with a thickness of 30 nm, where a substrate with low R_{sub} was prepared by applying the

double-layer AR coatings of Au and poly(methyl methacrylate) films to sufficiently thick Ag film on a substrate.[12] However, the reason why a thick Au film can be formed in the structure has not been discussed enough.

In addition, the surface material of the AR substrate for the visualization is currently limited to Au,[6, 11, 13–15] SiN_x,[7, 10, 16, 17] hBN,[18] and graphite.[18] Therefore, there has been little study on visualizing organic monolayer other than thiol monolayer on Au film with Au-S chemical bonds.[11, 12] Since organic monolayer are formed on a substrate with chemical bonding, there is potential to detect a variety of organic monolayers through the development of substrates with diverse materials on top. For instance, AR coatings with a SiO_2 surface could be utilized to detect an organosilicon monolayer that has been applied to electronic devices.[24, 25] Therefore, the development of a design technique for AR substrates with a layer of arbitrary materials on top is crucial for expanding the applications within surface science.

In contrast to the AR coatings for non-transparent substrates discussed above, multilayer AR coatings designed for transparent glass substrates are widely employed in various optical elements. Although the AR coatings are often constructed by stacking various transparent layers with different refractive indices and thicknesses, the theories and design techniques established for the AR coatings could offer valuable insights for the visualization study. The multilayer AR coatings have been developed using several theoretical approaches with the assistance of computer software.[26] One design approach involves the utilization of the reflection circle diagram, which visualizes the change in the complex reflection coefficient (ρ) at the front surface of the multilayer. In the method, each layer was assumed to build up on a previous layer in the final incident medium, and gradually grow in thickness from zero. In the process, the complex reflection coefficient continuously changed from the value of a base substrate (ρ_b) to the value of the final layer (ρ_{sub}) in

the multilayer. For visualizing the locus in the diagram, ρ at each stage of growth was individually calculated and plotted on a complex plane. The termination of the locus corresponds to ρ_{sub}. As R_{sub} of the designed multilayer is calculated as $|\rho_{sub}|^2$, $\rho_{sub} = 0$ is required for an ideal AR substrate. Therefore, AR coatings were designed by considering the visualized locus so that $|\rho_{sub}|$ became small.

Herein, we report the optical design of multilayer AR coatings using a reflection circle diagram. First, AR coatings that have been experimentally demonstrated for visualization were analyzed using the reflection circle diagram. Then, the design of AR coating with Au thin film on top and Cr adhesive layer underneath was discussed for depositing the ideal flat film. Furthermore, the graphical design of AR coatings with a layer of arbitrary materials on top was proposed, where the loci of examples are depicted in the circle diagram. Finally, the designed AR substrates with SiN_x and SiO_2 layers were experimentally fabricated, assessed by reflection spectroscopy, and used for visualizing monolayer and few-layer hBN flakes.

2. EXPERIMENTAL METHODS

2.1 Preparation

Si substrates coated with a 51 nm layer of SiN_x (Fuleda Technology) were cleaned by sonication in acetone and 2-propanol for 5 min in each. After treating the substrate with UV/ozone for 10 min for clearing, the SiO_2 film with a thickness of more than 100 nm was deposited at room temperature by radio-frequency sputtering at 400 W using a SiO_2 target. Then, the thickness of SiO_2 was adjusted to 20–60 nm by chemical etching of its surface with dilute HF at room

temperature. The bulk hBN crystals grown using a temperature-gradient method under a high-pressure and high-temperature atmosphere were used.[27] Ultra-thin hBN films were prepared by mechanical exfoliation with scotch tape and were immediately transferred to the substrate.

2.2 Characterization

The hBN flakes were identified through the 50× lens with NA of 0.8 (LU Plan 50×, Nikon) with a halogen lamp in an optical microscope (LV150, Nikon) and imaged using a monochrome 12 bit camera (CS-63M, Bitran) cooled to 10°C or a color 8 bit camera (EOS Kiss X4, Canon). To obtain superior images, the aperture stop was adjusted so that the light disk at the back focal plane of the lens was ~80% of that for fully open, which corresponds to a substantial reduction in NA. The reflectance spectra were measured using an optical microscope with a spectroscope (BTC-110S, B&W Tek) equipped at the trinocular head of the microscope. In contrast, the wavelength dependence was investigated with a narrow band-pass filter inserted in the optical path. The FWHM of the narrow band-pass filters was 10 nm. The morphology was studied using atomic force microscopy (AFM, NanoNavi, SII) in the tapping mode at room temperature in ambient air (50% relative humidity, ~20°C) with a Si cantilever (SI-DF3-R, SII Nano-Technology). The typical root-mean-square roughness of the SiO_2 surface was 0.2 nm. The thicknesses of SiN_x and SiO_2 film were determined based on spectra obtained by ellipsometry (Auto SE, Horiba) and/or reflectance spectroscopy.

3. CALCULATION MODEL

3.1 Calculation of reflection circle diagram.

Figure 1(a) shows the schematic of a multilayer substrate with p layers. $N = n - ik$ and d of each layer are complex refractive index and thickness, respectively, where i is an imaginary unit. N_m and N_b are refractive indices of an incident medium and base substrate, respectively, where N_m is 1.0 for air in the study; ρ_p corresponds to ρ_{sub} for substrate with p layers. In the construction, ρ continually changes from ρ_b to ρ_p. The changes at a growth stage are calculated sequentially. First, ρ_b is calculated by

$$\rho_b = \frac{N_m - N_b}{N_m + N_b}. \qquad (1)$$

Figure 1(b) shows the layer schematic in the middle of the deposition of the first layer, which corresponds to a single film with a thickness of d ($0 < d \leq d_1$). In this case, ρ is expressed as

$$\rho_1(d) = \frac{\rho_1^T + \rho_1^B exp(-2i\delta_1)}{1 + \rho_1^T \rho_1^B exp(-2i\delta_1)}, \qquad (2)$$

where $\delta_1 = 2\pi N_1 d_1/\lambda$, $\rho_1{}^T = (N_m - N_1)/(N_m + N_1)$ and $\rho_1{}^B = (N_1 - N_b)/(N_1 + N_b)$ are the reflection coefficients at the top and bottom boundaries, respectively.[19] The locus of ρ in the first layer is calculated by changing d. Similarly, the change in ρ for subsequent films is considered. **Figure 1(c)** is the layer schematic in the middle of qth-layer deposition with $0 < d \leq d_q$, where q is $1 < q < p$, and $\rho_q(d)$ is calculated using the transfer matrix method.[19, 20] The changes in the construction are calculated and plotted in the complex plane.[28] Although the above explanations are for normal incidence, ρ for oblique incidence is calculated similarly.[19, 20]

In the present study, ρ of the multilayer is discussed mainly at λ = 530 nm. The refractive indices of the employed materials at λ = 530 nm are listed in **Table 1**.[29–36] The refractive indices of SiO_2 and SiN_x were measured using the ellipsometer, whose wavelength dependence is shown in **Fig. S1**. The refractive index of hBN was assumed to be wavelength-independent, and the thickness of the hBN monolayer was set to 0.333 nm.[9]

3.2 Calculations of the locus of the final layer.

The R_{sub} of the completed multilayer substrate is given by $|\rho_p(d_p)|^2$, where $\rho_p(d_p)$ is the end of the locus of ρ for the final layer that corresponds to ρ_{sub}. As the locus of the final pth layer determines R_{sub}, the locus of $\rho_p(d)$ is important to consider for AR coatings. If the locus of the final layer passes through the origin of the diagram, a substrate with R_{sub} = 0 is obtained by adjusting d_p. This is performed by assuming a single layer on a virtual substrate with N_v that includes a (p–1) multilayer, as shown in **Fig. 1(d)**. Because this model contains a single coating, $\rho_p(d)$ is calculated by

$$\rho_p(d) = \frac{\rho_p^T + \rho_p^B \exp(-2i\delta_p)}{1 + \rho_p^T \rho_p^B \exp(-2i\delta_p)} \qquad (3)$$

as in **Eq. (2)**, where $\delta_p = 2\pi N_p d_p/\lambda$, $\rho_p{}^T = (N_m - N_p)/(N_m + N_p)$ and $\rho_p{}^B = (N_p - N_v)/(N_p + N_v)$ are the reflection coefficients at the top and bottom boundaries, respectively. Thus, the condition of $\rho_p(d_p) = 0$ for AR coating is

$$\rho_p^T + \rho_p^B \exp(-2i\delta_p) = 0. \qquad (4)$$

If **Eq. (4)** is rearranged, N_v may be expressed as

$$N_{\mathrm{v}} = \frac{(N_{\mathrm{p}}+1)\exp(-2i\delta_{\mathrm{p}})+(1-N_{\mathrm{p}})}{(N_{\mathrm{p}}+1)\exp(-2i\delta_{\mathrm{p}})-(1-N_{\mathrm{p}})} N_{\mathrm{p}}, \qquad (5)$$

indicating that N_{v} giving $\rho = 0$ is uniquely determined for the multilayer substrate with the top layer of a certain d_{p}. In this case, the reflectance of the virtual base substrate (ρ_{v}) corresponds to $\rho_{\mathrm{p}}(d)$, where ρ_{v} is calculated by $(N_{\mathrm{m}}-N_{\mathrm{v}})/(N_{\mathrm{m}}+N_{\mathrm{v}})$ similar to **Eq. (1)**. The locus of $\rho_{\mathrm{p}}(d) = \rho_{\mathrm{v}}$ is depicted in the circle diagram by changing d_{p} in $|\rho| \leq 1$.

3.3 Calculation of the reflectance spectra and contrast.

As the experimental reflectance spectra and photographs were acquired through the objective lens, the oblique incidence was taken into consideration in the calculation for comparison. When the incident light is tilted from the surface normal at an angle (θ), the measured $R(\lambda)$ is calculated as[11, 37]

$$R(\lambda) = \frac{1}{(\sin\theta_0)^2} \int_0^{\theta_0} (|\rho_{\mathrm{P}}(\lambda,\theta)|^2 + |\rho_{\mathrm{S}}(\lambda,\theta)|^2) \sin\theta\cos\theta d\theta, \qquad (6)$$

where $\rho_{\mathrm{P}}(\lambda, \theta)$ and $\rho_{\mathrm{S}}(\lambda, \theta)$ are the complex reflection coefficients for the P and S components of light, respectively, and θ_0 is defined by $\sin\theta_0$ = NA. The NA (numerical aperture) was set to 0.7 for all calculations, although the nominal NA of the objective used in the experiment is 0.8. This is because the aperture stop in the microscope limits the range of incident angle. The ρ_{P} (λ, θ) and $\rho_{\mathrm{S}}(\lambda, \theta)$ were calculated based on the multilayer model using the transfer matrix method described in **Sec. 3.1**.[19, 20]

The reflectance $\bar{R}(\lambda)$ of the ultra-thin hBN film detected by photographing with a narrow band-pass filter corresponds to the averaged reflectance for λ in the range of $\lambda' - \lambda_{\mathrm{FWHM}}/2$ to $\lambda' +$

$\lambda_{\mathrm{FWHM}}/2$, where λ' is a central wavelength of the filter, and λ_{FWHM} is the full width at half maximum (FWHM). The value of $\bar{R}(\lambda)$ was calculated by

$$\bar{R}(\lambda) = \frac{1}{\lambda_{\mathrm{FWHM}}} \int_{\lambda'-\lambda_{\mathrm{FWHM}}/2}^{\lambda'+\lambda_{\mathrm{FWHM}}/2} R(\lambda) d\lambda. \qquad (7)$$

The contrast of the flake with the substrate is defined by $C(\lambda) = \bar{R}_{\mathrm{f}}(\lambda)/\bar{R}_{\mathrm{sub}}(\lambda) - 1$. It is compared with the experimental contrast, which was calculated from the digital values in the image photographed by the monochrome camera[6, 7]

4. RESULTS AND DISCUSSION

4.1 Analysis of AR coatings by the reflection circle diagram

Figure 2 shows the reflection circle diagrams for five AR coatings that have been previously reported for visualizing ultra-thin films.[6, 7, 12, 18] The material and thickness of each layer are listed at the bottom of **Fig. 2**, with materials listed in the order from the substrate to the surface. Although the previous studies on the visualization technique were performed using AR coatings optimized for various wavelengths with objectives with different magnifications, the thickness of each film in **Fig. 2** was optimized so that R_{sub} for normal incidence became zero or minimum at 530 nm as initial analysis.

The AR films of (1) are composed of two insulating films.[18] The analytical studies for antireflection coatings with two insulator films on a non-transparent substrate have been reported.[38] The locus of ρ for (1) is **a**-**b**-**o** and starts from point **a**, which corresponds to ρ_{sub} of Si base substrate. Upon the deposition of the SiO_2 film, ρ goes to point **b** for the 19.4 nm deposition.

The termination of the first layer becomes the initial ρ for the following layer. The locus of ρ for the second hBN film starts continuously from point **b** and moves to the final point **o** for $|\rho| = 0$, i.e., $R = 0$. The circle, square, and triangle markers in **Fig. 2** indicate the movement of ρ in the circle diagram per unit thickness of 10, 5, and 1 nm for each layer, respectively.

When an insulating film is deposited on multilayer films, ρ moves along the circle whose center is on the real axis.[28] Then, it returns to the initial point by the deposition of the half-wave optical thickness film (181.1 nm and 120.5 nm for SiO_2 and hBN, respectively). The movement of ρ depends on N and the initial point of the locus.[28] The locus for an insulating film is analytically expressed in **Note S1**. Thus, the loci of **a-b** and **b-o** are parts of each circle.

AR coatings (2) and (3) are composed of an insulating film and an absorbing film with $k \neq 0$.[12, 18] The locus of ρ for an absorbing layer generally becomes complicated compared with a non-absorbing layer with $k = 0$.[28] In the case of (2), the locus of ρ starts from point **a** for the Si base substrate as in case (1) and goes through point **b** to point **c** for a 76.3 nm SiO_2 film. The arc is longer than in case (1) because of additional deposition. Then, for a 6.0 nm graphite film, ρ moves to point **o**. The movement of ρ for graphite per unit thickness is larger than SiO_2 or hBN layer. Generally, the movement of an absorbing film is larger than that of a non-absorbing film, suggesting that strict thickness control is required for AR coating. The locus of ρ for (3) is **e-f-o**. The locus starts from point **e** for the Ag-based substrate. The $|\rho|$ of point **e** is larger than that of point **a**. This is because R for the Ag-based substrate is higher than that for the Si-based substrate at 530 nm. As a result, a large circle is observed in the circle diagram for an insulating film on the Ag substrate.

AR coating (4) includes Cr adhesive layer for Au film.[6] The locus can be understood that the adhesive layer was added to cases (2) or (3). Point **g** for Si/SiO_2 (112.2 nm)/Cr (0.5 nm) is on the locus of **f**-**o** for (3). Then, they reach **o** point on the same locus upon the deposition of the Au film of appropriate thickness.

AR coating (5) is a single-layer coating.[7, 16, 17] Theoretically, the deposition of a single film with N, which optically matches a non-transparent substrate makes R zero at a certain λ.[39, 40] The refractive index of SiN_x is close to the ideal value for Si.[7] Therefore, the termination point **h** in the locus corresponds to R = 0.28%, which is suitable for the visualization of ultra-thin films.[7]

4.2 Effect of adhesive layer for top Au layer in multilayer AR coatings

The reflection circle diagram is useful for investigating the effect of the adhesive layer for the top Au layer, particularly in the substrate/non-absorbing layer/adhesive layer/Au structure. **Figure 3(a)** shows the reflection circle diagram for a SiO_2/Cr/Au AR coating on different substrates at 530 nm. The thickness of the Cr layer was fixed at 0.5 nm, whereas the thickness of the Au layer was optimized. The blue solid line corresponds to case (4) in **Fig. 2**. The loci start from ρ_{sub} of each base substrate. For comparison, ρ_{sub} of various base substrates is plotted with black dots. The locus of the SiO_2 film becomes a circular arc, with the radius increasing with substrate R, as explained in case (3) in **Fig. 2**. The locus of Au film for the three substrates is on the broken ochre-colored curve. As described in **Sec. 2.2**, the locus of Au film which passes through $\rho = 0$ is uniquely determined irrespective of the substrate before Au deposition (here, the substrate is named $p-1$ substrate). In other words, designing an AR coating with an Au surface requires the terminating point of the previous layer (Cr layer in the case) to be on the curve. In the

case of a base substrate with SiO_2/Cr coatings, this requirement is satisfied by adjusting the thickness of the SiO_2 film. Once ρ of a $p-1$ substrate is on the curve, AR coating with $\rho = 0$ can be obtained by depositing an Au film with appropriate thickness. The thickness of the Au film for $\rho = 0$ is 8.3, 14.8, and 23.4 nm for Ag, Cu, and Si base substrates, respectively. The thickness of the Au film for $\rho = 0$ increases with $|\rho|$ of a $p-1$ substrate. This becomes a practical advantage for depositing a homogeneous, flat, and stable Au thin film.[21–23]

Figure 3(b) shows the Ag/SiO_2/Cr/Au substrate with different thicknesses of the Cr adhesive layer. The blue, red, and black solid lines correspond to the Cr layer thickness of 3.0, 1.5, and 0.5 nm, respectively. Numerically, the thickness of the Au film for $\rho = 0$ is 7.6, 16.7, and 23.4 nm, respectively. Therefore, a thin Cr adhesive layer is preferred from the point of view of depositing a continuous and flat Au film.

The broken curve in **Fig. 3(a)** represents the additional Au deposition on the AR substrates. The reflectance increased along the curve and finally corresponded to ρ of the base Au substrate. This corresponds to an increase of d_p for the Au layer in **Eq. (3)**. The δ_p in **Eq. (3)** can be expanded as $\delta_p = 2\pi N_p d_p/\lambda = 2\pi(n_p - ik_p)d_p/\lambda = 2\pi n_p d_p/\lambda - i2\pi k_p d_p/\lambda$. Here, the first term represents the phase change, while the second term represents attenuation due to the absorption of light. Since light decays exponentially in absorbing layers, an increase of thickness in an absorbing layer sensitively changes ρ in the circular diagram toward the bulk value of ρ_b. Consequently, $\rho_p(d)$ for a sufficiently thick Au film is equal to $\rho_p{}^T$ in **Eq. (3)** due to the complex N_p, corresponding to **Eq. (1)** for a bulk Au substrate.

4.3 Oblique incidence in multilayer AR coatings

When ultra-thin films are photographed through a high-magnification objective with large NA, oblique incidence in multilayer AR coatings must be considered. The locus of reflectance in the circle diagram varies with incidence angle and polarization. [19] The black solid line in **Fig. 4** corresponds to the locus of the case (4) in **Fig. 2**. The red and blue solid line indicates the locus of S- and P-polarized incidence at an incidence angle of 44° at $\lambda = 530$ nm. Numerically, the incidence angle corresponds to θ_0, where $\sin\theta_0 = 0.7$ is the NA of the objective. The broken gray circles indicate $|\rho| = 0.7$, 0.5, 0.3, and 0.1. Although the behavior of ρ for polarization is similar to the normal incidence, the loci are terminated not in the origin. Therefore, the reflection light for the AR coating which is experimentally detected through the lens does not become zero numerically, resulting in the reduction of visibility.[7, 15, 20] The circular diagram can graphically explain the effects of oblique incidence and evaluate the AR coatings.

The optical design of AR coatings for microscopic observation of ultra-thin films requires a substrate with low reflectance regardless of the incident angle. Research into the effect of variations in incidence angle on AR coatings has been conducted.[41–45] The AR coatings for an oblique incident can be designed in the same way as for normal light with the circle diagram by including the effect of the incident angle in the refractive index of each layer, where the phase change attributed to the incidence angle is corrected.[19, 41]

Although the AR coating design proposed in this study can be adapted to polarized oblique incidence with a certain angle, it is difficult to design the AR coating considering the sum of reflections from various incident angles collected by the objective. Further analytical studies are needed to improve the visibility of microscopic observations. However, AR substrates optimized

for normal incidence have been practically applied to microscopic observation with objectives with high NA.[6–10, 14–18, 20] Therefore, the present study primarily focused on normal incidence.

4.4 Design of an AR coating

The discussion of AR coating with Au surface can be generalized to the design of an AR coating with a layer of an arbitrary material on top. First, the design of AR coating with a surface of absorbing material is elaborated on. The light-gray, dark-gray, orange, ochre, and red curves in **Fig. 5(a)** indicate the loci of Cr, Ti, Cu, Au, and Al passing through $\rho = 0$, respectively. The broken curves represent the additional deposition on the AR coatings. The broken black circle indicates $|\rho| = 1$. For an AR coating, the termination of ρ of a $p-1$ substrate must be on the curve of the desired metallic material. Once the termination is on the line, $\rho = 0$ can be achieved by adjusting the thickness of the final metallic film. Thus, the position control of the termination of the $(p-1)$ substrate is the key to the design of AR coatings. Here let us focus on the single-layer coating of non-absorbing material on an absorbing base substrate. The structure has already been discussed in **Fig. 3(a)** for a thin layer of SiO_2 on various substrates. The termination point of the SiO_2 layer can be freely controlled in a wide range in the circle diagram by adjusting the SiO_2 thickness and selecting the R of the base substrate (details are explained in **Note S1** and **Fig. S4**). Therefore, a substrate with a single-layer coating of non-absorbing material is useful for the $(p-1)$ substrate. Specific examples for the AR substrate with Ti and Cu on the surface are represented with red and blue solid lines in **Fig. 5(b)**, respectively, where AR coating can be designed by optimizing the thickness of the non-absorbing layer and the metallic film.

The described method may be applied to the design of AR coatings with a non-absorbing material on the surface. The blue, purple, pink, and green markers in **Fig. 5(a)** indicate the loci of TiO_2, Al_2O_3, polymethyl methacrylate (PMMA), and SiO_2 passing through $\rho = 0$, respectively. Deposition of a non-absorbing film with a half-wave optical thickness traces a complete circle clockwise.[28] The depicted loci of the five metals (Cr, Ti, Cu, Au, and Al) pass through the four circles and intersect at $\rho \neq 0$. Several arrangements can be considered using the loci of absorbing materials. As the circle of non-absorbing materials intersects with the curves at $\rho = 0$, AR coatings can be obtained by the deposition of a non-absorbing film with a half-wave optical thickness on a substrate with AR coating with $\rho = 0$. An example of AR coating of Ni/SiO_2/Cr/PMMA is shown in **Fig. 5(b)** with the orange solid line, where the Ni substrate with SiO_2/Cr coatings was used as a $p-1$substrate. The locus of PMMA starts from the origin and traces the circle clockwise. It then returns to the origin at a half-wave optical thickness.

The other intersections of the locus of an absorbing material at $\rho \neq 0$ are useful. AR coating is also obtained by depositing a non-absorbing film with a thickness that corresponds to the intersection of the $p-1$ substrate with ρ. An example Si/PMMA/Cr/Al_2O_3 AR coating is shown in **Fig. 5(b)** with the green solid line. Although the locus of Cr intersects with the circle of Al_2O_3 at $\rho = 0$, the thickness of Cr film is additionally increased until the next intersection. Then, Al_2O_3 film with a thickness that satisfies $\rho = 0$ is deposited on the $p-1$substrate.

The other arrangement that does not use the loci of absorbing materials can be considered. The solid black line in **Fig. 5(b)** corresponds to Al/Al_2O_3/Ti/TiO_2. The locus of the Ti layer does not pass through the origin. By adjusting the thickness of Al_2O_3 and Ti, the termination of the locus of Ti may be positioned on the circle of TiO_2. Then, the deposition of TiO_2 film with an appropriate thickness on the $(p-1)$ substrate affords $\rho = 0$. Because the loci of metals, which do not pass

through the origin, are generally complicated, the assistance of computer software is required.[28] As shown in the examples, the device structure of metal substrate/insulator/metal/insulator has been applied to an infrared absorber for solar thermophotovoltaic systems.[46]

4.5 Demonstration

The demonstration was performed on the double-layer SiN_x and SiO_2 film, where SiO_2 film was sputtered on a Si substrate with a SiN_x film. The black solid line in **Fig. 6(a)** shows the locus of the AR coating of $Si/SiN_x/SiO_2$ for normal incidence at 530 nm. Theoretically, the perfect AR coating can be obtained with the two layers.[38] The broken black line in **Fig. 6(a)** indicates the locus of Si/SiN_x without the SiO_2 layer for comparison, which corresponds to the locus of the case (5) in **Fig. 2**. It is considered that part of the SiN_x film is replaced with SiO_2 film. The substrate with the double-layer AR coatings with lower R is expected to improve the visualization of ultra-thin films. The red and blue solid line in **Fig. 6(a)** shows the circle diagram for S- and P-polarized incidence at an incidence angle of 44° at λ = 530 nm, similar to **Fig. 4**. **Figure 6(b)** shows the reflection spectra of the AR coatings with different SiO_2 thicknesses measured through the 50× objective lens. The calculations indicated by the broken line for NA = 0.7 roughly reproduce the experimental spectra in both cases. Microscopic observation with high visibility is expected from the reflection spectra of low reflectance even with a high-magnification objective.

Finally, the performance of the visualization technique for the AR coating was evaluated on ultra-thin hBN flakes. The visibility of the monolayer hBN film has been well known to be poor because of its optical transparency and atomic-scale thickness of 0.333 nm.[9] **Figure 7** is the data set for monolayer and few-layer hBN flakes on Si/SiN_x (50 nm)/SiO_2 (25 nm). **Figure 7(a) and**

(b) shows the photograph taken through the 50× objective lens with monochrome and color cameras at λ = 470 nm at the same position, respectively. **Figure 7(c)** is the photograph in white light. Notably, images in **Fig. 7(b) and 7(c)** were not processed (the contrast was not increased). The numbers in **Fig. 7(a)** indicate the layer number determined by AFM. The monolayer hBN flakes on the substrate are recognized in all images even in white light. However, the use of an appropriate narrow band-pass filter enhances the contrast of the ultra-thin flakes.

Figures 7(d) and (e) respectively show the phase and height images obtained via tapping-mode AFM of the monolayer corresponding to the red square area in **Fig. 7(a)**. **Figure 7(f)** shows the profile of average height along the white solid bold line in **Fig. 7(e)**. The height step of 0.4−0.5 nm indicates a monolayer film.[47, 48] Although the height image does not show a sufficient topographical difference for the monolayer, the phase image shows the clear boundary of the monolayer flake by the phase difference of ~5 degrees between the hBN and bare substrate. This feature is useful for AFM measurements. The lag of the phase difference is independent of the layer number, suggesting that the phase shift might be related to the mechanical properties of hBN, such as stiffness or elastic modulus.[49, 50] The AFM data for different numbers are shown in **Fig. S3**.

Figure 7(g) shows the contrast spectra of 1–4 layers (L) for the hBN flakes of **Fig. 7(a–c)**. Peaks are observed in positive contrast at λ = ~470 nm and negative contrast at λ = ~530 nm for all layers. The broken lines represent the calculation results for NA = 0.7, which roughly reproduce the experiment. **Figure 7(h)** shows the contrast depending on the layer number at λ = 450, 470, 600, and 630 nm, which corresponds to **Fig. 7(g)**. As shown by the calculation results (broken lines), the contrast increases almost linearly with increasing layer number from zero.[51] The experimental contrast is roughly consistent with the calculations for all layers, and the intercept

for each layer is near zero. This confirms the determination of the layer number by the optical contrast and AFM measurement. The maximum absolute contrast of the monolayer is 17% at 470 nm. Because the monochrome camera used in the present experimental setup practically detects the contrast of 3% for ultra-thin films, the height resolution of the visualization technique is calculated to be 59 pm from the estimate of monolayer thickness.

The effect of the designed double-layer AR coating is further discussed. The maximum absolute contrast of an hBN monolayer in the observation with a narrow band-pass filter has been reported to be 15% for the Si substrate with a single-layer AR coating of SiN_x.[7] The improved contrast was attributed to the lower R of the substrate. The reflection and contrast spectra are compared in **Fig. S4**. As shown in **Fig. 7(c)**, the monolayer flakes on the double-layer AR coating may be directly identified without an optional optical filter and image processing, which is helpful to find monolayer flakes from a large number of flakes with different thicknesses placed randomly on the substrate in live-view mode of the camera. At the same time, image processing for improving the contrast is required to recognize a monolayer on the single-layer AR coating of SiN_x.

The improvement in contrast contributes to the layer number determination. In the case of the substrate with single-layer AR coating of SiN_x, a narrow band-pass filter must be carefully selected for the observation at an appropriate wavelength because only a limited number of wavelengths may be used for detection.[7] Furthermore, the suitable wavelength sensitively changes with the SiN_x thickness because the reflective index of SiN_x is higher than that of SiO_2. Thus, strict control of the SiN_x thickness or the use of a large number of narrow band-pass filters with a variety of wavelengths is required. However, if the double-layer AR coating is applied, a narrow band-pass filter for a variety of wavelengths in the visible region may be used for the layer number determination, as shown in **Fig. 7(h)**. Compared with the measurements of electrical tunneling

current [6, 52, 53] or Raman shift [9, 47, 54], which have been used to determine the number of layers, the proposed method can determine the number of layers quickly, accurately, and non-destructively.

5. CONCLUSION

Research on AR substrates for visualizing ultra-thin films was carried out using the reflection circle diagram, which graphically visualizes the continuous change in ρ during the construction of multilayer AR coatings. First, the AR coatings that have been developed in previous research were analyzed. The loci of the AR coatings with optimized layer thickness for normal incidence at λ = 530 nm started from ρ of the base substrate and finished at or near $\rho = 0$. Since the change of ρ with increasing layer thickness in the circle diagram is determined by the refractive index of each layer, the behavior of ρ serves as a guideline for optimizing the film thickness of each layer. Specifically, the effect of the adhesive layer on the structure of absorbing-substrate/non-absorbing-layer/Cr/Au was discussed to increase the thickness of the top Au layer. The optimized thickness of the top Au layer increases with increasing R_b of a base substrate and decreasing Cr layer thickness. Therefore, the use of a base substrate with a larger R_b and thinner Cr adhesive layer is suggested to obtain a flat and stable Au top layer. Furthermore, the reflection circle diagram-based design of an AR multilayer substrate was proposed. The design technique enables the development of AR substrates with arbitrary materials on top by combining about 3 layers of non-absorbing-layer and absorbing-layer. These AR substrates might be widely used not only for visualization of ultra-thin films, but also for detecting slight changes in surface properties and nanostructures.

Finally, the experimental demonstration with double-layer AR coating of SiN_x and SiO_2 film was performed. The reflection spectra of the designed AR coating measured through the lens roughly correspond to the calculation results. The performance of the visualization technique was assessed on monolayer and few-layer hBN films. As a result, the monolayer hBN films on Si/SiN_x (50 nm)/SiO_2 (25 nm) were identified in the image with the maximum optical contrast of 17% at λ = 470 nm. The AR coating enables direct observation without an optical filter and image processing and affords easy determination of the layer number.

FIGURES

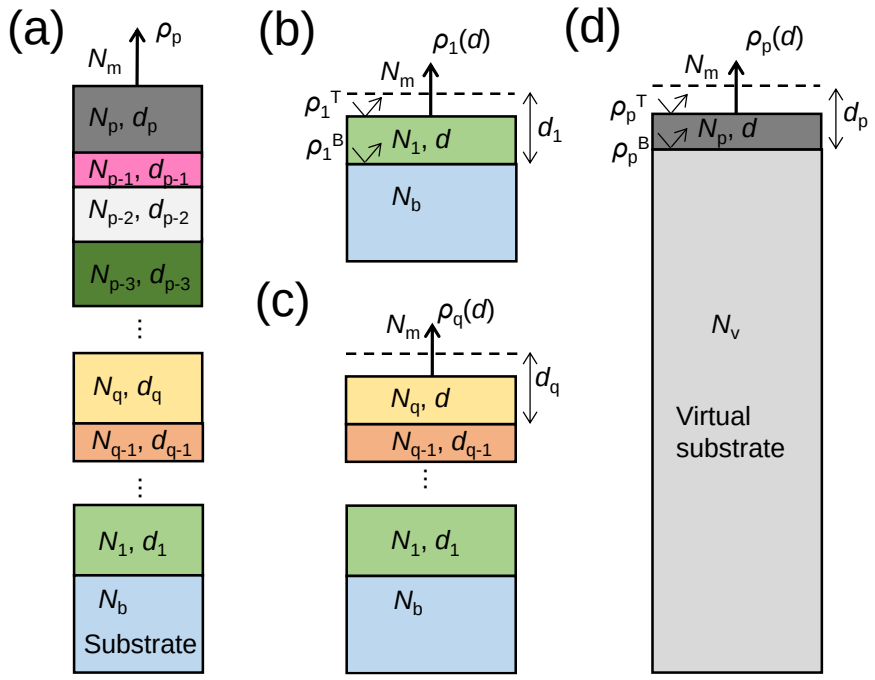

Figure 1: Multilayer calculation model. **(a)** Model for multilayer substrate with p layers. **(b, c)** Models of the middle of the first and qth-layer deposition, respectively. **(d)** Model of a substrate with single-layer on the virtual substrate that includes p–1 multilayer for calculating the locus of the final layer passing through $\rho = 0$.

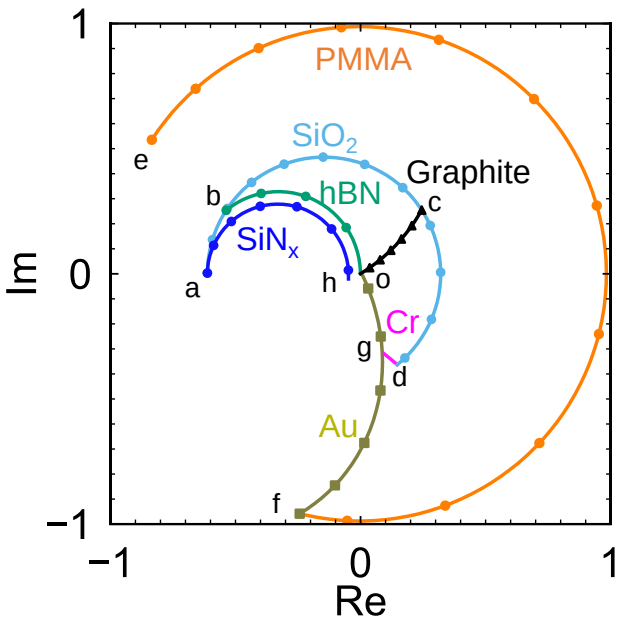

(1) Si/SiO_2 (19.4 nm)/hBN (38.8 nm) a-b-o
(2) Si/SiO_2 (76.3 nm)/Graphite (6.0 nm) a-c-o
(3) Ag/PMMA (105.4 nm) /Au (27.0 nm) e-f-o
(4) Si/SiO_2 (112.2 nm)/Cr (0.5 nm) /Au (8.3 nm) a-d-g-o
(5) Si/SiN_x (62.0 nm) a-h

Figure 2: Reflection circle diagram of various AR coatings at λ = 530 nm. The structures of AR substrates are listed at the bottom of the figure, with layers written in the order from the substrate to the surface. Lowercase alphanumeric characters connected by hyphens in the list indicate loci. The thickness of each layer is adjusted so that R for normal incidence becomes zero or minimum. The round, square, and triangle markers indicate the movement of ρ in the loci associated with each deposition per unit thickness of 10, 5, and 1 nm, respectively.

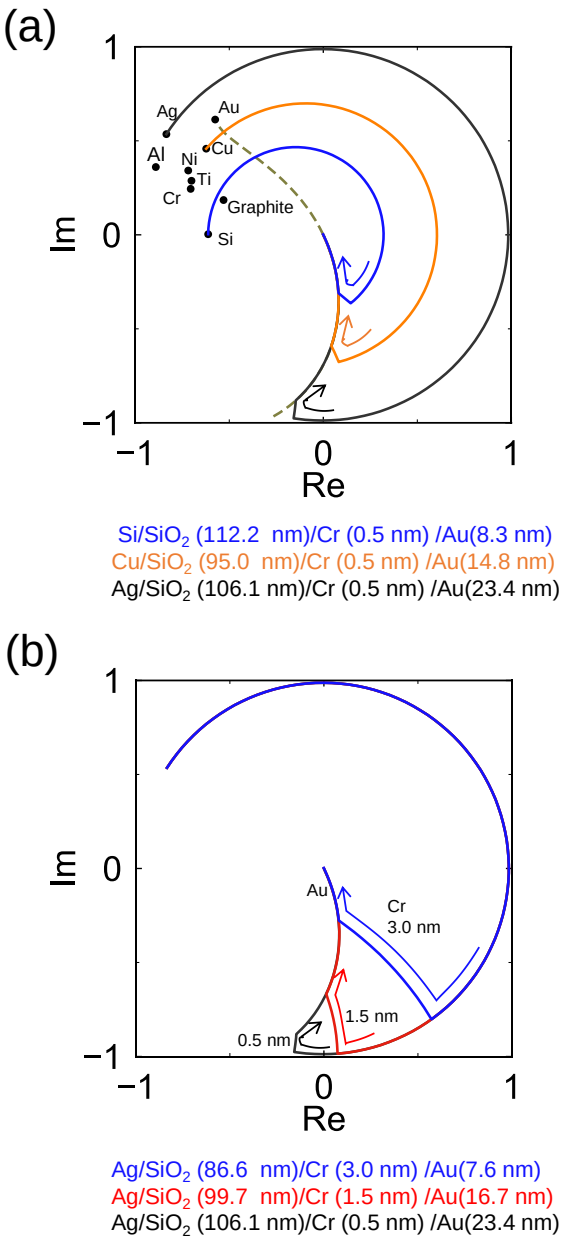

Figure 3: **(a)** Reflection circle diagram of the SiO_2/Cr/Au AR coating at λ = 530 nm with different base substrates for normal incidence. The black dots indicate the ρ_{sub} of various base substrates. The broken ochre curve indicates the locus of Au film which passes through ρ = 0. **(b)** Reflection circle diagram of the Ag/SiO_2/Cr/Au substrate at λ = 530 nm with different base substrates. A base substrate with a large R and a thin Cr layer is preferred for the structure from the viewpoint of continuous and flat Au film deposition.

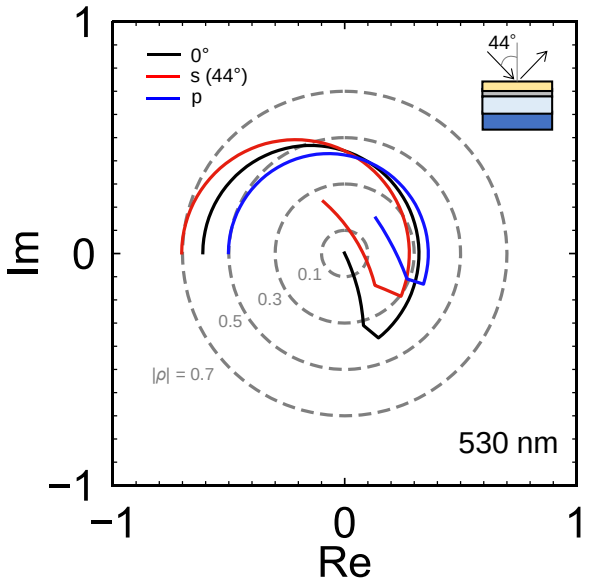

Figure 4: Circle diagram of the AR coating of (4) in **Fig. 2** for S- and P-polarized incidence at a incidence angle of 44° at λ = 530 nm.

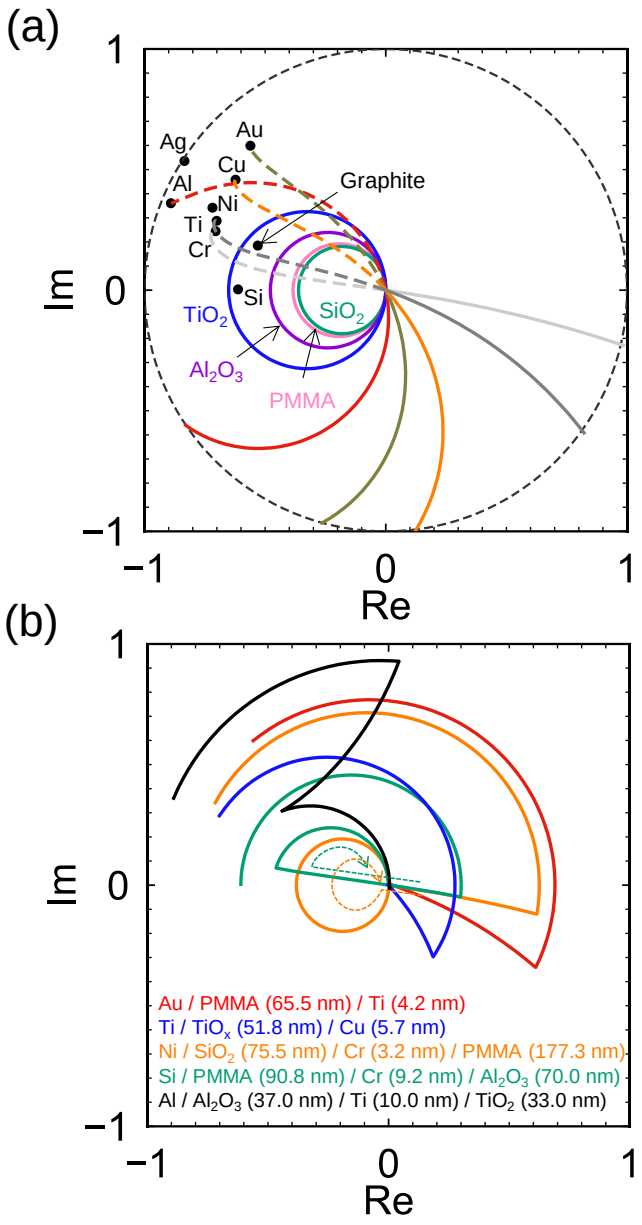

Figure 5: **(a)** Loci of various materials in multilayer coating passing through $\rho = 0$ in the circle diagram. **(b)** Loci of AR substrates with Ti, Cu, PMMA, Al_2O_3, TiO_2 surface as examples for designing AR coating with a top layer of arbitrary materials.

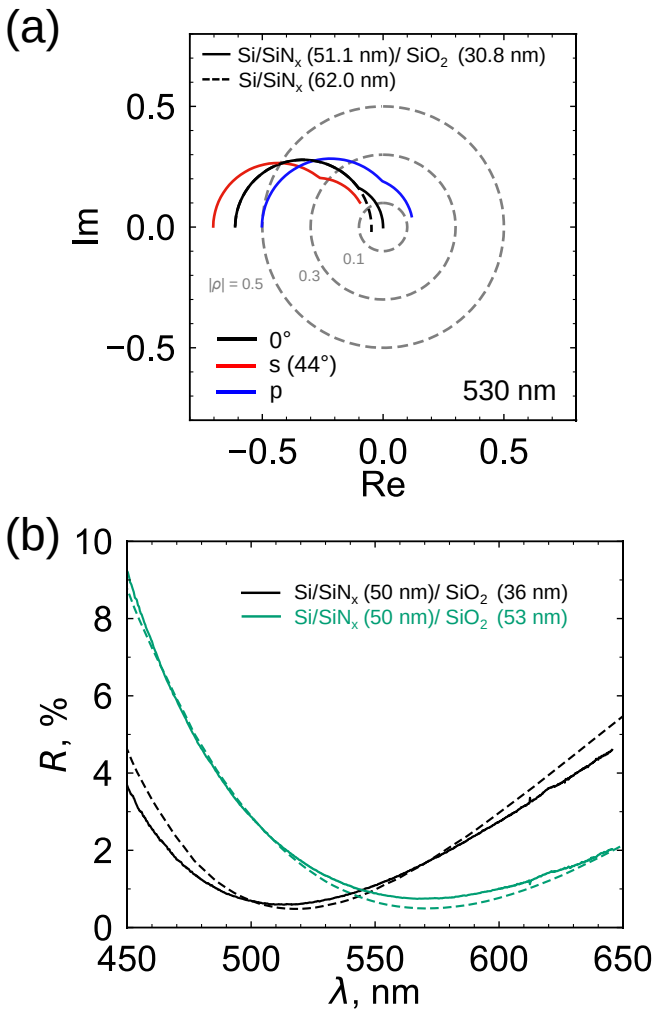

Figure 6: **(a)** Circle diagram of the Si/SiN_x/SiO_2 AR coating for S- and P-polarized incidence at a incidence angle of 44° at λ = 530 nm. **(b)** Reflection spectra of the Si/SiN_x/SiO_2 AR coatings with different SiO_2 thicknesses.

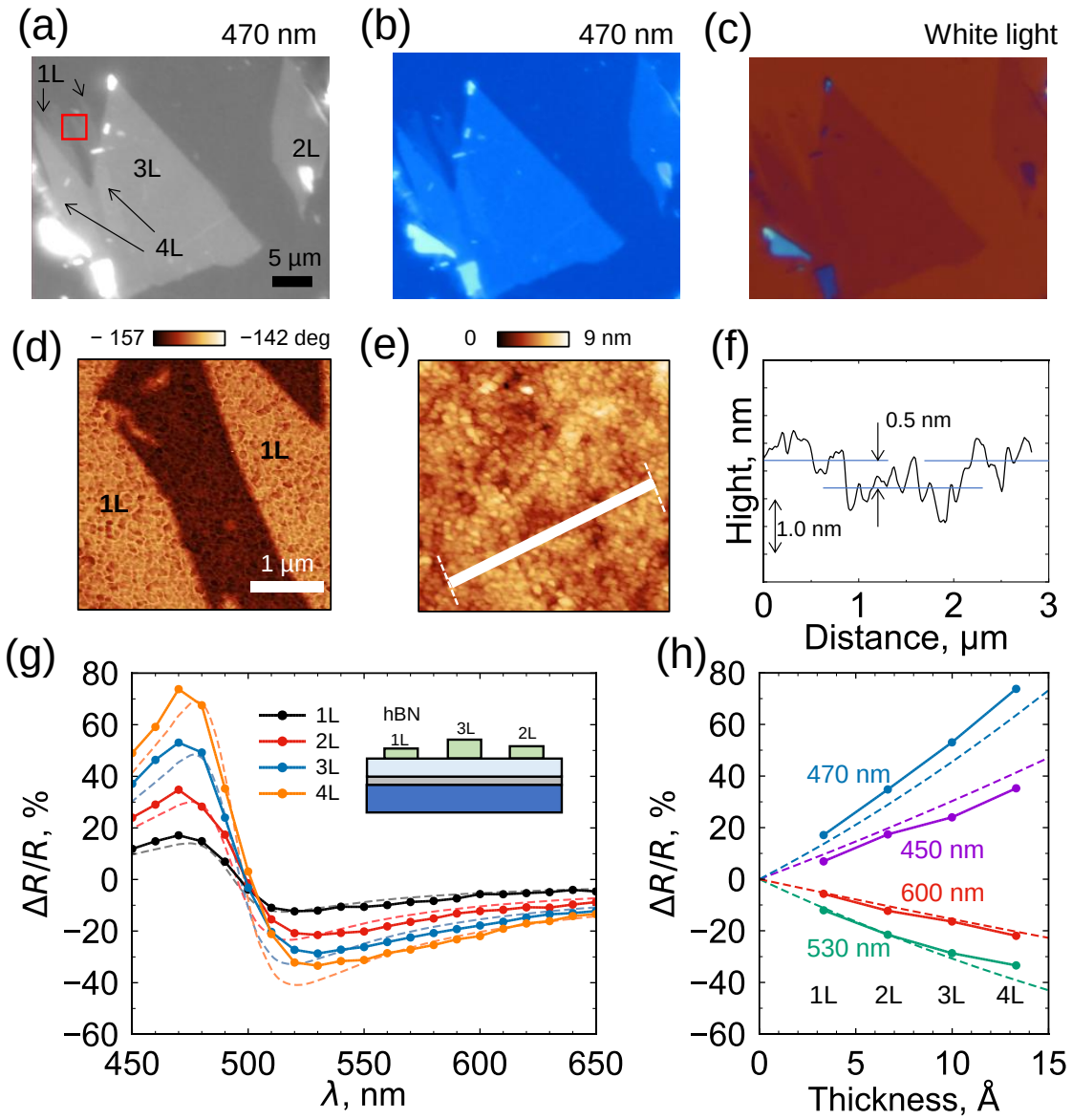

Figure 7: Characterization of monolayer and few-layer hBN flakes on Si/SiN_x (50 nm)/SiO_2 (25 nm). (**a**) and (**b**) Monochromatic and color photographs at λ = 530 nm, respectively. (**c**) Color photograph in white light. **(d)** and **(e)** Phase and height tapping-mode AFM images of the monolayer corresponding to the red square area in **(a)**, respectively. **(f)** The profile of average height along the white solid bold line in **(e)**. The broken white lines in (**e**) indicate the area of the averaged height profile. (**g**) Contrast spectra of 1−4 layers of hBN film on the substrate. The dots

and broken lines indicate experimental and calculation results, respectively. **(h)** Contrast depending on the layer number at λ = 450, 470, 530, and 600 nm.

TABLE

Table 1: List of refractive indices at λ = 530 nm for materials used in the study.

Materials	Refractive indices
Air	1.000 – *i* 0.000
Si	4.159 – *i* 0.043 [29]
SiO_2	1.463 – *i* 0.000
SiN_x	2.156 – *i* 0.015
PMMA	1.495 – *i* 0.000 [30]
hBN	2.200 – *i* 0.000 [9]
TiO_2	2.176 – *i* 0.000 [31]
Al_2O_3	1.684 – *i* 0.000 [32]
Au	0.592 – *i* 2.173 [33]
Ag	0.054 – *i* 3.410 [34]
Cr	3.023 – *i* 3.334 [35]
Ti	2.475 – *i* 3.342 [35]
Cu	1.143 – *i* 2.601 [34]
Al	0.540 – *i* 5.081 [36]
Ni	1.871 – *i* 3.483 [35]
Graphite	2.600 – *i* 1.300 [8]

ASSOCIATED CONTENT

A list of the contents in Supporting Information.

Analytical description of the locus of a non-absorbing layer in the circle diagram, refractive index of SiO_2 and SiN_x, loci of various non-absorbing layers in the circle diagram, AFM phase and height images for 1−4 L hBN, and reflection and contrast spectra for Si/SiN_x and $Si/SiN_x/SiO_2$ substrate.

AUTHOR INFORMATION

Corresponding Author

Email: hattori@eedept.kobe-u.ac.jp (Y. Hattori), kitamura@eedept.kobe-u.ac.jp (M. Kitamura)

Notes

The authors declare no competing financial interests.

ACKNOWLEDGMENT

This work was partly supported by JSPS KAKENHI Grant Numbers 21K04195, 21H04655, Kansai Research Foundation, Chubei Itoh Foundation, Iketani Science and Technology Foundation, and Hyogo Science and Technology Association.

REFERENCES

(1) Hoffmann, H.; Mayer, U.; Brunner, H.; Krischanitz, A. Reflection-Absorption Infrared Spectroscopy of Self-Assembled Monolayers on Gold and Silicon Surfaces. *Vibrational Spectroscopy* **1995**, *8* (2), 151–157. https://doi.org/10.1016/0924-2031(94)00037-H.

(2) Wasserman, S. R.; Whitesides, G. M.; Tidswell, I. M.; Ocko, B. M.; Pershan, P. S.; Axe, J. D. The Structure of Self-Assembled Monolayers of Alkylsiloxanes on Silicon: A Comparison of Results from Ellipsometry and Low-Angle x-Ray Reflectivity. *J. Am. Chem. Soc.* **1989**, *111* (15), 5852–5861. https://doi.org/10.1021/ja00197a054.

(3) Shi, J.; Hong, B.; Parikh, A. N.; Collins, R. W.; Allara, D. L. Optical Characterization of Electronic Transitions Arising from the Au/S Interface of Self-Assembled *n*-Alkanethiolate Monolayers. *Chemical Physics Letters* **1995**, *246* (1), 90–94. https://doi.org/10.1016/0009-2614(95)01085-N.

(4) Ikematsu, N.; Takahashi, H.; Hattori, Y.; Kitamura, M. Formation of a Mixed Monolayer on a Gold Surface Using Fluorobenzenethiol and Alkanethiol. *Jpn. J. Appl. Phys.* **2019**, *59* (SD), SDDA09. https://doi.org/10.7567/1347-4065/ab4ebc.

(5) Takahashi, H.; Ikematsu, N.; Hattori, Y.; Kitamura, M. Formation of a Monolayer on a Gold Surface with High Thermal Stability Using Benzenedithiol. *Jpn. J. Appl. Phys.* **2019**, *59* (SD), SDDA03. https://doi.org/10.7567/1347-4065/ab51ce.

(6) Hattori, Y.; Taniguchi, T.; Watanabe, K.; Kitamura, M. Visualization of a Hexagonal Boron Nitride Monolayer on an Ultra-Thin Gold Film via Reflected Light Microscopy. *Nanotechnology* **2022**, *33* (6), 065702. https://doi.org/10.1088/1361-6528/ac3357.

(7) Hattori, Y.; Taniguchi, T.; Watanabe, K.; Kitamura, M. Enhancement of the Contrast for a Hexagonal Boron Nitride Monolayer Placed on a Silicon Nitride/Silicon Substrate. *Appl. Phys. Express* **2022**, *15* (8), 086502. https://doi.org/10.35848/1882-0786/ac8270.

(8) Blake, P.; Hill, E. W.; Castro Neto, A. H.; Novoselov, K. S.; Jiang, D.; Yang, R.; Booth, T. J.; Geim, A. K. Making Graphene Visible. *Applied Physics Letters* **2007**, *91* (6), 063124. https://doi.org/10.1063/1.2768624.

(9) Gorbachev, R. V.; Riaz, I.; Nair, R. R.; Jalil, R.; Britnell, L.; Belle, B. D.; Hill, E. W.; Novoselov, K. S.; Watanabe, K.; Taniguchi, T.; Geim, A. K.; Blake, P. Hunting for Monolayer Boron Nitride: Optical and Raman Signatures. *Small* **2011**, *7* (4), 465–468. https://doi.org/10.1002/smll.201001628.

(10) Jung, I.; Pelton, M.; Piner, R.; Dikin, D. A.; Stankovich, S.; Watcharotone, S.; Hausner, M.; Ruoff, R. S. Simple Approach for High-Contrast Optical Imaging and Characterization of Graphene-Based Sheets. *Nano Lett.* **2007**, *7* (12), 3569–3575. https://doi.org/10.1021/nl0714177.

(11) Hattori, Y.; Takahashi, H.; Ikematsu, N.; Kitamura, M. Chain-Length Dependence of Optical Properties for an Alkanethiol Monolayer on an Ultrathin Gold Film Revealed via Reflected Light Microscopy. *J. Phys. Chem. C* **2021**, *125* (27), 14991–14999. https://doi.org/10.1021/acs.jpcc.1c03080.

(12) Syahir, A.; Kajikawa, K.; Mihara, H. Sensitive Detection of Small Molecule–Protein Interactions on a Metal–Insulator–Metal Label-Free Biosensing Platform. *Chemistry – An Asian Journal* **2012**, *7* (8), 1867–1874. https://doi.org/10.1002/asia.201200138.

(13) Hattori, Y.; Kitamura, M. Reflected Light Microscopy of a Gold Oxide Layer Formed on a Au Film by Ultraviolet/Ozone Treatment. *Thin Solid Films* **2023**, *764*, 139631. https://doi.org/10.1016/j.tsf.2022.139631.

(14) Velický, M.; Donnelly, G. E.; Hendren, W. R.; McFarland, S.; Scullion, D.; DeBenedetti, W. J. I.; Correa, G. C.; Han, Y.; Wain, A. J.; Hines, M. A.; Muller, D. A.; Novoselov, K. S.; Abruña, H. D.; Bowman, R. M.; Santos, E. J. G.; Huang, F. Mechanism of Gold-Assisted Exfoliation of Centimeter-Sized Transition-Metal Dichalcogenide Monolayers. *ACS Nano* **2018**, *12* (10), 10463–10472. https://doi.org/10.1021/acsnano.8b06101.

(15) Donnelly, G. E.; Velický, M.; Hendren, W. R.; Bowman, R. M.; Huang, F. Achieving Extremely High Optical Contrast of Atomically-Thin MoS_2. *Nanotechnology* **2020**, *31* (14), 145706. https://doi.org/10.1088/1361-6528/ab6237.

(16) Rubio-Bollinger, G.; Guerrero, R.; De Lara, D. P.; Quereda, J.; Vaquero-Garzon, L.; Agraït, N.; Bratschitsch, R.; Castellanos-Gomez, A. Enhanced Visibility of MoS_2, $MoSe_2$, WSe_2 and Black-Phosphorus: Making Optical Identification of 2D Semiconductors Easier. *Electronics* **2015**, *4* (4), 847–856. https://doi.org/10.3390/electronics4040847.

(17) An, J. Y.; Kahng, Y. H. Optical Observation of Single Layer Graphene on Silicon Nitride Substrate. *AIP Advances* **2018**, *8* (1), 015107. https://doi.org/10.1063/1.5009821.

(18) Hattori, Y.; Taniguchi, T.; Watanabe, K.; Kitamura, M. Identification of the Monolayer Thickness Difference in a Mechanically Exfoliated Thick Flake of Hexagonal Boron Nitride and Graphite for van Der Waals Heterostructures. *Nanotechnology* **2023**. https://doi.org/10.1088/1361-6528/accf23.

(19) MacLeod, H. A.; Macleod, H. A. *Thin-Film Optical Filters*; CRC Press, 2010.

(20) Casiraghi, C.; Hartschuh, A.; Lidorikis, E.; Qian, H.; Harutyunyan, H.; Gokus, T.; Novoselov, K. S.; Ferrari, A. C. Rayleigh Imaging of Graphene and Graphene Layers. *Nano Lett.* **2007**, *7* (9), 2711–2717. https://doi.org/10.1021/nl071168m.

(21) Smith, G. B.; Niklasson, G. A.; Svensson, J. S. E. M.; Granqvist, C. G. Noble‐metal‐based transparent infrared reflectors: Experiments and theoretical analyses for very thin gold films. *Journal of Applied Physics* **1986**, *59*(2), 571−581. https://doi.org/10.1063/1.336615.

(22) Todeschini, M.; Bastos da Silva Fanta, A.; Jensen, F.; Wagner, J. B.; Han, A. Influence of Ti and Cr Adhesion Layers on Ultrathin Au Films. *ACS Appl. Mater. Interfaces* **2017**, *9* (42), 37374–37385. https://doi.org/10.1021/acsami.7b10136.

(23) Yakubovsky, D. I.; Arsenin, A. V.; Stebunov, Y. V.; Fedyanin, D. Y.; Volkov, V. S. Optical Constants and Structural Properties of Thin Gold Films. *Opt. Express, OE* **2017**, *25* (21), 25574–25587. https://doi.org/10.1364/OE.25.025574.

(24) Shtein, M.; Mapel, J.; Benziger, J. B.; Forrest, S. R. Effects of Film Morphology and Gate Dielectric Surface Preparation on the Electrical Characteristics of Organic-Vapor-Phase-Deposited Pentacene Thin-Film Transistors. *Applied Physics Letters* **2002**, *81* (2), 268–270. https://doi.org/10.1063/1.1491009.

(25) Yang, H.; Shin, T. J.; Ling, M.-M.; Cho, K.; Ryu, C. Y.; Bao, Z. Conducting AFM and 2D GIXD Studies on Pentacene Thin Films. *J. Am. Chem. Soc.* **2005**, *127* (33), 11542–11543. https://doi.org/10.1021/ja052478e.

(26) Thelen, A. Design of Optical Minus Filters. *J. Opt. Soc. Am., JOSA* **1971**, *61* (3), 365–369. https://doi.org/10.1364/JOSA.61.000365

(27) Watanabe, K.; Taniguchi, T.; Kanda, H. Direct-Bandgap Properties and Evidence for Ultraviolet Lasing of Hexagonal Boron Nitride Single Crystal. *Nature Mater* **2004**, *3* (6), 404–409. https://doi.org/10.1038/nmat1134.

(28) Apfel, J. H. Graphics in Optical Coating Design. *Appl. Opt., AO* **1972**, *11* (6), 1303–1312. https://doi.org/10.1364/AO.11.001303.

(29) Palik, E. D. *Handbook of Optical Constants of Solids: Volume 1*; Academic Press, Boston, 1985, pp. 547–569

(30) Beadie, G.; Brindza, M.; Flynn, R. A.; Rosenberg, A.; Shirk, J. S. Refractive Index Measurements of Poly(Methyl Methacrylate) (PMMA) from 0.4–1.6 Mm. *Appl. Opt., AO* **2015**, *54* (31), F139–F143. https://doi.org/10.1364/AO.54.00F139.

(31) Sarkar, S.; Gupta, V.; Kumar, M.; Schubert, J.; Probst, P. T.; Joseph, J.; König, T. A. F. Hybridized Guided-Mode Resonances via Colloidal Plasmonic Self-Assembled Grating. *ACS Appl. Mater. Interfaces* **2019**, *11* (14), 13752–13760. https://doi.org/10.1021/acsami.8b20535.

(32) Boidin, R.; Halenkovič, T.; Nazabal, V.; Beneš, L.; Němec, P. Pulsed Laser Deposited Alumina Thin Films. *Ceramics International* **2016**, *42* (1, Part B), 1177–1182. https://doi.org/10.1016/j.ceramint.2015.09.048.

(33) Rakić, A. D.; Djurišić, A. B.; Elazar, J. M.; Majewski, M. L. Optical Properties of Metallic Films for Vertical-Cavity Optoelectronic Devices. *Appl. Opt., AO* **1998**, *37* (22), 5271–5283. https://doi.org/10.1364/AO.37.005271.

(34) Johnson, P. B.; Christy, R. W. Optical Constants of the Noble Metals. *Phys. Rev. B* **1972**, *6* (12), 4370–4379. https://doi.org/10.1103/PhysRevB.6.4370.

(35) Johnson, P. B.; Christy, R. W. Optical Constants of Transition Metals: Ti, V, Cr, Mn, Fe, Co, Ni, and Pd. *Phys. Rev. B* **1974**, *9* (12), 5056–5070. https://doi.org/10.1103/PhysRevB.9.5056.

(36) Cheng, F.; Su, P.-H.; Choi, J.; Gwo, S.; Li, X.; Shih, C.-K. Epitaxial Growth of Atomically Smooth Aluminum on Silicon and Its Intrinsic Optical Properties. *ACS Nano* **2016**, *10* (11), 9852–9860. https://doi.org/10.1021/acsnano.6b05556.

(37) Lu, Y.; Li, X.-L.; Zhang, X.; Wu, J.-B.; Tan, P.-H. Optical Contrast Determination of the Thickness of SiO_2 Film on Si Substrate Partially Covered by Two-Dimensional Crystal Flakes. *Science Bulletin* **2015**, *60* (8), 806–811. https://doi.org/10.1007/s11434-015-0774-3.

(38) Cox, J. T. Special Type of Double-Layer Antireflection Coating for Infrared Optical Materials with High Refractive Indices. *J. Opt. Soc. Am., JOSA* **1961**, *51* (12), 1406–1408. https://doi.org/10.1364/JOSA.51.001406.

(39) Hass, G.; Schroeder, H. H.; Turner, A. F. Mirror Coatings for Low Visible and High Infrared Reflectance*. *J. Opt. Soc. Am., JOSA* **1956**, *46* (1), 31–35. https://doi.org/10.1364/JOSA.46.000031.

(40) Park, K. C. The Extreme Values of Reflectivity and the Conditions for Zero Reflection from Thin Dielectric Films on Metal. *Appl. Opt., AO* **1964**, *3* (7), 877–881. https://doi.org/10.1364/AO.3.000877.

(41) Turbadar, T. Equi-Reflectance Contours of Triple-Layer Anti-Reflection Coatings. *Optica Acta: International Journal of Optics* **1964**, *11* (3), 195–205. https://doi.org/10.1080/713817881.

(42) Cox, J. T.; Hass, G.; Thelen, A. Triple-Layer Antireflection Coatings on Glass for the Visible and Near Infrared. *J. Opt. Soc. Am., JOSA* **1962**, *52* (9), 965–969. https://doi.org/10.1364/JOSA.52.000965.

(43) Apfel, J. H. Electric Fields in Multilayers at Oblique Incidence. *Appl. Opt., AO* **1976**, *15* (10), 2339–2343. https://doi.org/10.1364/AO.15.002339.

(44) Apfel, J. H. Graphical Method to Design Multilayer Phase Retarders. *Appl. Opt., AO* **1981**, *20* (6), 1024–1029. https://doi.org/10.1364/AO.20.001024.

(45) Catalán, L. A. Some Computed Optical Properties of Antireflection Coatings. *J. Opt. Soc. Am., JOSA* **1962**, *52* (4), 437–440. https://doi.org/10.1364/JOSA.52.000437.

(46) Shimizu, M.; Kohiyama, A.; Yugami, H. Evaluation of Thermal Stability in Spectrally Selective Few-Layer Metallo-Dielectric Structures for Solar Thermophotovoltaics. *Journal of Quantitative Spectroscopy and Radiative Transfer* **2018**, *212*, 45–49. https://doi.org/10.1016/j.jqsrt.2018.02.037.

(47) Li, L. H.; Cervenka, J.; Watanabe, K.; Taniguchi, T.; Chen, Y. Strong Oxidation Resistance of Atomically Thin Boron Nitride Nanosheets. *ACS Nano* **2014**, *8* (2), 1457–1462. https://doi.org/10.1021/nn500059s.

(48) Cui, X.; Shih, E.-M.; Jauregui, L. A.; Chae, S. H.; Kim, Y. D.; Li, B.; Seo, D.; Pistunova, K.; Yin, J.; Park, J.-H.; Choi, H.-J.; Lee, Y. H.; Watanabe, K.; Taniguchi, T.; Kim, P.; Dean, C. R.; Hone, J. C. Low-Temperature Ohmic Contact to Monolayer MoS_2 by van Der Waals Bonded Co/h-BN Electrodes. *Nano Lett.* **2017**, *17* (8), 4781–4786. https://doi.org/10.1021/acs.nanolett.7b01536.

(49) Magonov, S. N.; Elings, V.; Whangbo, M.-H. Phase Imaging and Stiffness in Tapping-Mode Atomic Force Microscopy. *Surface Science* **1997**, *375* (2), L385–L391. https://doi.org/10.1016/S0039-6028(96)01591-9.

(50) García, R.; Pérez, R. Dynamic Atomic Force Microscopy Methods. *Surface Science Reports* **2002**, *47* (6), 197–301. https://doi.org/10.1016/S0167-5729(02)00077-8.

(51) Huang, F. Optical Contrast of Atomically Thin Films. *J. Phys. Chem. C* **2019**, *123* (12), 7440–7446. https://doi.org/10.1021/acs.jpcc.8b12333.

(52) Lee, G.-H.; Yu, Y.-J.; Lee, C.; Dean, C.; Shepard, K. L.; Kim, P.; Hone, J. Electron Tunneling through Atomically Flat and Ultrathin Hexagonal Boron Nitride. *Appl. Phys. Lett.* **2011**, 99 (24), 243114. https://doi.org/10.1063/1.3662043.

(53) Britnell, L.; Gorbachev, R. V.; Jalil, R.; Belle, B. D.; Schedin, F.; Katsnelson, M. I.; Eaves, L.; Morozov, S. V.; Mayorov, A. S.; Peres, N. M. R.; Castro Neto, A. H.; Leist, J.; Geim, A. K.;

Ponomarenko, L. A.; Novoselov, K. S. Electron Tunneling through Ultrathin Boron Nitride Crystalline Barriers. *Nano Lett.* **2012**, *12* (3), 1707–1710. https://doi.org/10.1021/nl3002205.

(54) Li, L. H.; Santos, E. J. G.; Xing, T.; Cappelluti, E.; Roldán, R.; Chen, Y.; Watanabe, K.; Taniguchi, T. Dielectric Screening in Atomically Thin Boron Nitride Nanosheets. *Nano Lett.* **2015**, *15* (1), 218–223. https://doi.org/10.1021/nl503411a.